Deep–Sea Research II 200 (2022) 105094

Contents lists available at ScienceDirect

Deep-Sea Research Part II

journal homepage: www.elsevier.com/locate/dsr2

Optical particle measurements reveal cross-shelf turbidity gradients on the Agulhas Bank

Sarah L.C. Giering [a,*], Margaux Noyon [b], Brian Godfrey [b], Alex J. Poulton [c], Filipa Carvalho [a], Mike Roberts [a,b]

[a] Ocean Biogeosciences, National Oceanography Centre, Southampton, United Kingdom
[b] Nelson Mandela University, Gqeberha, South Africa
[c] The Lyell Centre, Heriot-Watt University, Edinburgh, United Kingdom

ARTICLE INFO

Keywords:
Turbidity
Benthic nepheloid layer
Agulhas bank
Resuspension
Particles

ABSTRACT

The Agulhas Bank is a moderately productive and dynamic shelf ecosystem. In this region, underwater visibility can, at times, be poor owing to high turbidity near the seabed. However, it is currently unclear what causes high-turbidity events and how far they extend. Using an analysis of optical particle data (backscatter and fluorescence), we show a strong cross-shelf gradient of near-bottom turbidity and distinct particle dynamics across the study region. The region near Port Alfred was characterized by high levels of new production and vertical transport of organic matter to depth via sinking particles. On the Central Agulhas Bank, our observations were consistent with the suggestion of particle retention owing to a larger cyclonic recirculation pattern. Close to the coast we observed four sites with benthic nepheloid layers (BNL) that were likely formed because of resuspension of sediments. Our data indicate that there was no instantaneous link between BNL and sinking phytodetritus, though a time lag between export events and benthic remineralization could have obscured a direct link between surface productivity and BNL formation.

1. Introduction

The marine ecosystem around South Africa is one of the most diverse in the world owing to complex ocean circulation. Particularly, upwelling of deep Antarctic and Indian Ocean waters and the strong Benguela and Agulhas Currents allow for high biodiversity and ocean productivity (Hutchings et al., 2009). South Africa's marine environment can be broadly divided into three biogeographical regions: the warm subtropical east coast, the temperate shelf in the southeast (Agulhas Bank; focus of this paper), and the cold west coast. The Agulhas Bank is a productive temperate shelf the whole year round (Demarcq et al., 2008; Mazwane et al., this issue), an important spawning ground for many fish species, and supports economically important commercial fisheries; yet it is a threatened habitat in terms of overfishing, resource exploitation and climate change (Sink et al., 2012). High turbidity (high concentrations of suspended particulate matter) is frequent on the Agulhas Bank (Jackson et al., 2012; Roberts and Sauer, 1994; Zoutendyk and Duvenage, 1989). Anecdotal evidence of high turbidity events is provided by fishermen and SCUBA divers who observed very turbid waters near the coast, for example, at intermediate depths (~ 10–20 m depth; Shaun Deyzel, pers. comm., 2021) or near the seabed with, at times, near-zero visibility (Mike Roberts, pers. comm., 2021). High turbidity events have been suggested to change squid population dynamics by reducing mating success (Roberts and Sauer, 1994). Yet, it is currently unclear what causes these high turbidity events on the Agulhas Bank and how far they extend.

The ecosystem of the Agulhas Bank is strongly influenced by the east-west Agulhas Current, which brings warm waters from the Indian Ocean and flows along the shelf edge. Along the shelf, the Agulhas Current drives persistent shelf-break upwelling, pushing nutrient-rich water onto the shelf (Jackson et al., 2012; Goschen et al., 2015). Along the coast from Port Alfred to Plettenberg Bay, wind-driven coastal upwelling occurs (Schumann and Brink, 1990; Goschen et al., 2015). As the Agulhas Bank widens south of Port Elizabeth (now Gqeberha), the Agulhas Current starts to meander. These meanders (of which solitary ones are referred to as Natal Pulses) can move waters onshore and drive an intermittent coastal countercurrent along the coast (Gründlingh, 1979; Harris et al., 1978; Lutjeharms and Roberts, 1988; Krug and

* Corresponding author.
E-mail address: s.giering@noc.ac.uk (S.L.C. Giering).

https://doi.org/10.1016/j.dsr2.2022.105094
Received 20 January 2021; Received in revised form 23 February 2022; Accepted 13 April 2022
Available online 29 April 2022

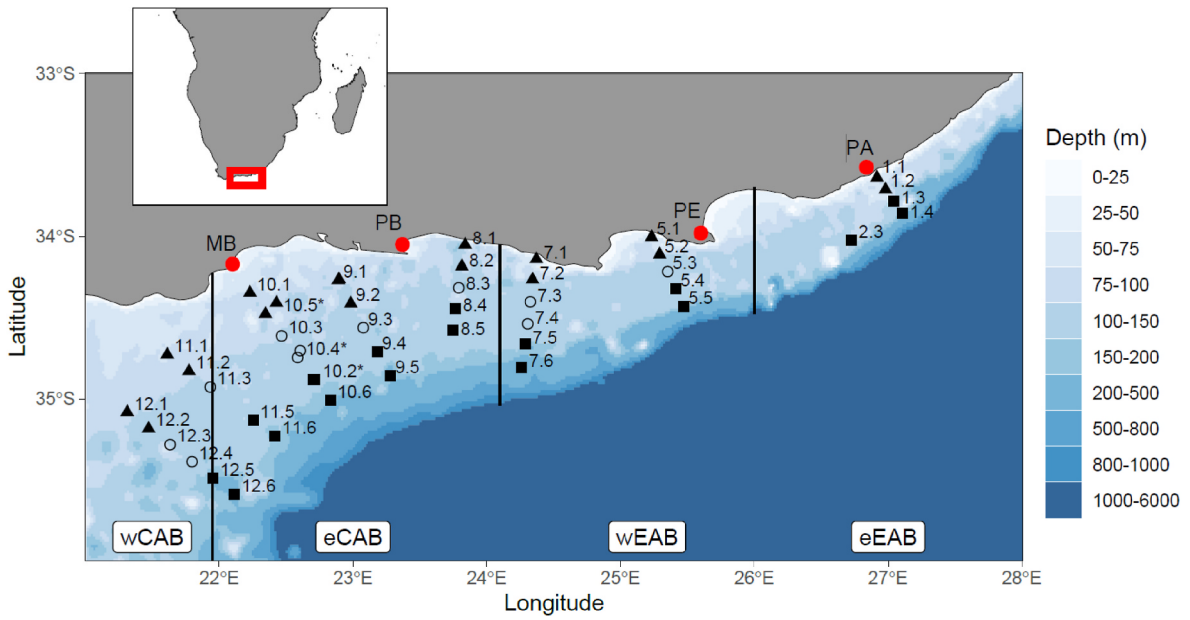

Fig. 1. Sites sampled during this study. Stations are named (TT.S) indicating the transect (TT) and inshore-offshore position (S, with 1 being closest to the shore). Colours show bathymetry (see colour bar; in m). Symbols indicate inshore (solid triangle), mid-shore (open circle) and offshore (solid square) stations. The extent of the study regions are indicated by the horizontal bars: western Central Agulhas Bank (wCAB), eastern Central Agulhas Bank (eCAB), western Eastern Agulhas Bank (wEAB), and eastern Eastern Agulhas Bank (eEAB). *Three sites (CR1, CR3 and CR4), located respectively near station 10.2, 10.4 and 10.5, were revisited towards the end of the cruise. (PA: Port Alfred, PE: Port Elizabeth (now Gqeberha), PB: Plettenberg Bay, MB: Mossel Bay) Cape Agulhas).

Penven, 2011; Goschen et al., 2015; Malan et al., 2018). On the Central Agulhas Bank, the divergent westward flow of the Agulhas Current along the outer shelf coupled to the wind-driven eastwards coastal current has been suggested to cause a persistent cyclonic retention cell (Boyd and Shillington, 1994; Hutchings 1994; Miller et al., 2006). In addition, internal solitary waves are known to occur on the Agulhas Bank (Boegman and Stastna, 2019; Jackson, 2004), which are key drivers of sediment movement on continental slopes and have been shown to cause both bottom and intermediate nepheloid layers (Boegman and Stastna, 2019; Tian et al., 2019, 2021a, 2021b). In the complex hydrographic system of the Agulhas Bank, we expect a strong influence of the resuspension of sedimentary matter on near-bottom turbidity (Gardner et al., 2018).

While the hydrography of the Agulhas Bank is fairly well studied, little information exists on the amount of organic matter that sinks out of the productive surface ocean (no known publications). Surface Chlorophyll-*a* (Chl) is often high on the Agulhas Bank (Carter et al., 1987; Probyn et al., 1994), suggesting that organic matter export from the productive surface could also be high. Such exported matter can accumulate near the seabed and increase turbidity (Lampitt, 1985). Given its dynamic nature, this coastal region has high spatiotemporal variability in phytoplankton productivity and physiology (Carter et al., 1987; Poulton et al., this issue) that could lead to high fluxes of sinking organic matter and, subsequently, high near-bottom turbidity.

Turbidity events are characterized by high suspended particle concentrations (e.g. Townsend et al., 1992, and references herein) that can be identified by measuring the absorption or transmission of light shining through the water. With the recent development of energy-efficient high-brightness light-emitting diodes (LED) and highly sensitive photodetectors, the optical properties of the water column (e.g., transmission and backscatter) can be measured at high spatiotemporal resolution. Moreover, high-resolution turbidity measurements can be paired with other optical measurements to provide in-depth insights into the water column dynamics. For example, backscatter intensity has been shown to be strongly correlated with organic matter concentrations in the open ocean, and can hence be used to quantify particulate organic matter (subject to site-specific calibration) (Cetinić et al., 2012). Fluorescence sensors (LED: 470 nm, photodetector: 695 nm) can be used to quantify algal pigments, such as Chl concentrations (Lorenzen, 1966). Large particles (>100 μm in diameter) in the optical sampling volume of these absorption and transmission sensors cause spikes in the signal, and these spikes can be used to quantify large particle concentrations (Briggs et al., 2011), to estimate particle size spectra (Briggs et al., 2013), and to infer particle fragmentation rates (Briggs et al., 2020).

The combination of backscatter and fluorescence signals can be used to infer the composition of the particle assemblage (Barbieux et al., 2018; Schallenberg et al., 2019), similar to the use of the ratio of in situ Chl to particulate organic carbon (POC) to infer algal physiology and ecosystem dynamics (Moore et al., 2007). Alongside the inherent phytoplankton Chl-to-POC ratio, which varies with physiology, the composition of POC is complex, with phytoplankton, zooplankton, bacteria and detrital material all contributing. In productive ecosystems (e.g., spring blooms), much of the POC will be from phytoplankton so that Chl:POC ratios are high. As productivity declines (deep in the water column or post-bloom), more heterotrophs and detritus contribute to the POC pool, resulting in lower Chl:POC ratios. In near-shelf regions or areas with high dust-input, the interpretation of the backscatter signal is less clear as resuspension and terrestrial particulate matter ('lithogenic matter') can lead to high turbidity in the water, and hence to higher backscatter signals, without an increase in POC concentrations (Stramski et al., 2004).

In this study, we use vertical profiles of optical measurements, collected during a survey in March 2019, to determine the extent of high turbidity regions on the Agulhas Bank. We hypothesise that we can use the combination of backscatter (at 532 and 700 nm) and fluorescence sensors to characterize the vertical structure of the water over the Agulhas Bank and determine different ecological regimes within the study region. We further hypothesise that high-turbidity events on the Agulhas Bank have distinct optical signatures that reflect their origin and can hence indicate whether they are caused by resuspended sediments or settling organic matter.

2. Methods

2.1. Study site

We investigated the Eastern Agulhas Bank during 19 Mar – Apr 2, 2019 aboard the *R.V. Ellen Khuzwayo* (voyage EK188). Our survey (Fig. 1; Supplementary Table 1) started in the east near Port Alfred (closest station: 33.64°S, 29.92°E) and followed the general circulation towards the west of the bank (most western station: 35.10°S, 21.31°E). Based on Chl and nitrate concentrations during our survey, the surface waters experienced different stages of the phytoplankton bloom, ranging from 'post-bloom' to 'pre-bloom' to 'non-bloom' (Poulton et al., this issue). Size-fractionated Chl measurements during our survey showed that nanoplankton (2–20 μm) dominated the phytoplankton community on the bank, though microplankton (>20 μm) contributions increased to the west (Poulton et al., this issue). Our sampling strategy was to collect samples along cross-shelf transects covering the full width of the shelf, with the nomenclature being as follows: transects were numbered successively from east to west (transects 1–12) and stations from inshore to offshore (1–6). Each station had a unique 'grid' number, corresponding to 'transect.station' (from 1.1 to 12.6; see Fig. 1). Three additional profiles were collected at long-term ADCP mooring locations (CR1, CR3 and CR4; Hancke et al., this issue). A full description of the EK188 cruise and its CTD deployments can be found in the cruise report (Noyon, 2019).

Across the programme, the Agulhas Bank was divided into the Central Agulhas Bank (CAB) and Eastern Agulhas Bank (EAB) at 24°E. For this study, we further separated each region into a western and an eastern part. The CAB was sectioned along 22°E so that the western CAB (wCAB) includes stations 12.1–12.4 and 11.1–11.3 and the eastern CAB (eCAB) includes stations 12.4–12.5, 11.4–11.6 and transects 10 and 9. The EAB was sectioned along 26°E, with the western EAB (wEAB) covering transects 5–8, and the eastern EAB (eEAB) covering transects 1–2. We further distinguished inshore and offshore stations as the two inner stations (stations 1 and 2) and the two outer stations of each transect. The water column depths of inshore and offshore stations were, generally, <100 m and >100 m, respectively.

The depth of the surface mixed layer was determined as the depth of the maximum buoyancy frequency, or N^2 (Carvalho et al., 2017), between the surface and a density layer that is 0.8 kg m^{-3} higher than the surface (see also Poulton et al., this issue). This definition allows the separation of the upper ocean from the bottom-influenced dynamics and the identification of a mixed layer that is varying in similar timescales to the phytoplankton community (Carvalho et al., 2017). The depth of the bottom mixed layer depth was determined using two different density thresholds (0.01 and 0.02 kg m^{-3}) from the bottom density value (Hopkins et al., 2021). All density profiles were visually checked to make sure the surface and bottom mixed layers were correctly detected and that the former was matching the shape of the Chl fluorescence (used as a proxy for phytoplankton biomass). Nutrients (nitrite, nitrate, phosphate and silicate) and dissolved oxygen concentrations were sampled and analysed as described by Poulton et al. (this issue).

2.2. ECO triplet

A 1000-m rated standalone Seabird Environmental Characterization Optics (ECO) Triplet Fluorometer and Backscattering Sensor, measuring Chl fluorescence (excitation/emission at 470/695 nm) and backscatter at two wavelengths in the green and red spectrum (532 nm and 700 nm, respectively, at 124°), was used during the cruise. The setup was similar to the sensors on one of the gliders used during this field campaign (Seaglider SG550, fitted with 700 nm, CDOM and fluorescence). The ECO Triplet was deployed on the CTD rosette, fitted horizontally and facing outward. This instrument did not have a pressure sensor, and it thus relied on the depth sensor of the Seabird CTD on the rosette, which was matched using time stamps (see below). The ECO Triplet and depth sensors were aligned on the same plane, and the offset between the two sensors was <10 cm. The ECO Triplet was mounted onto the CTD frame for the entirety of the EK188 cruise and set to self-logging using internal storage. Data was sampled at a rate of 10 Hz and extracted using the EcoView123 software.

Table 1
Sensor calibration details. Serial number: BB2FLWB-1633. Calibration Date: Sep 2017. *Dark blanks determined Jun 2018.

	ECO Chlorophyll Fluorometer	Scattering meter at 700 nm	Scattering meter at 532 nm
Scale Factor	0.0626 μg L^{-1} $count^{-1}$	3.004×10^{-6} (m^{-1} sr^{-1}) $count^{-1}$	6.974×10^{-6} (m^{-1} sr^{-1}) $count^{-1}$
Dark Blank*	47 ± 5 counts	62 ± 6 counts	27 ± 5 counts
Noise	±0.313 μg L^{-1}	$\pm 1.80 \times 10^{-5}$ m^{-1} sr^{-1}	$\pm 3.49 \times 10^{-5}$ m^{-1} sr^{-1}

Chlorophyll: Chl (μg L^{-1}) = Scale Factor x (Output-Dark Blank).
Backscatter: b_{bp} (m^{-1} sr^{-1}) = Scale Factor x (Output-Dark Blank).

All data rows containing corrupted data and values outside the sensor range, as defined by the manufacturer, were removed. The ECO Triplet clock was synced with the ship server time (GPS GMT) before the first deployment and not changed thereafter. Upon recovery, we detected a difference between the ship server time, the time of the CTD unit and the ECO Triplet, caused by an unexpected drift in the sensor's internal clock. To determine the drift, we initially roughly matched CTD data (>10 m depth) and ECO Triplet data based on the apparent date and time. We then calculated the correlations (linear regression) between fluorescence and turbidity (700 nm) from the CTD vs the fluorescence and backscatter (700 nm) from the ECO Triplet, with a range of potential time delays (0–12 s). The most likely time delay was determined as the delay with the highest R^2. We identified a consistent drift (0.72 s day^{-1}) in the ECO Triplet's internal clock ($p < 0.001$, $R^2 = 0.60$, $n = 94$) and applied this regression to assign the correct sampling depth.

The scale factor for Chl (0.0626 μg Chl L^{-1} $count^{-1}$) was determined during the cruise ($p < 0.001$, $R^2 = 0.58$, $n = 152$) with discrete Chl measurements. Briefly, seawater samples were collected using 10-L Niskin bottles on the CTD rosette sampler between 2 m and 80 m water depth. Seawater (200 mL) was filtered through Whatman GF/F filters (25 mm diameter, 0.7 μm nominal pore size), and Chl extracted in 6 mL 90% acetone (Sigma-Aldrich, UK) for 18–24 h (in darkness at 4 °C). Chl fluorescence was measured using a fluorometer (Turner-Designs Trilogy™, US) using a non-acidification module (Welschmeyer, 1994) calibrated with solid and pure Chl standards (Sigma-Aldrich, UK).

ECO Triplet counts were converted into the volume scattering function ($\beta(\theta)$, m^{-1} sr^{-1}) using the manufacturer-supplied scale factor (Table 1) and dark blanks determined for the instrument (median signal recorded between 400 and 1000 m depth in the open ocean 9 months before the cruise; cruise DY090 in Jun 2018). Sensor drift was likely minimal during our 2-week study as indicated by a second set of dark blanks determined for the instrument 8 months after this study (cruise DY111 in Dec 2019). Dark blanks were not different to each other (mean ± standard deviation. Chl: 47 ± 5 vs 49 ± 3, bp532: 27 ± 5 vs 26 ± 4, and bp700: 62 ± 6 vs 56 ± 3). Volume scattering was converted into integrated particulate backscattering (b_{bp}) by subtracting the scattering of pure seawater (Zhang et al., 2009) and using a χ conversion factor of 1.077 (Sullivan et al., 2013). The noise of the sensor (standard deviation of dark blank) was equivalent to 3.49×10^{-5} m^{-1} sr^{-1}, 1.80×10^{-5} m^{-1} sr^{-1} and 0.31 μg Chl L^{-1} for 532 nm, 700 nm and fluorescence, respectively (Table 1). Data are available (https://doi.org/10.5285/d9567f7a-ba96-683a-e053-6c86abc0ab7e).

2.3. Spike analysis

Small and large particles were determined following the methods by Briggs et al. (2011). Particulate backscattering (b_{bp}) was partitioned into two components:

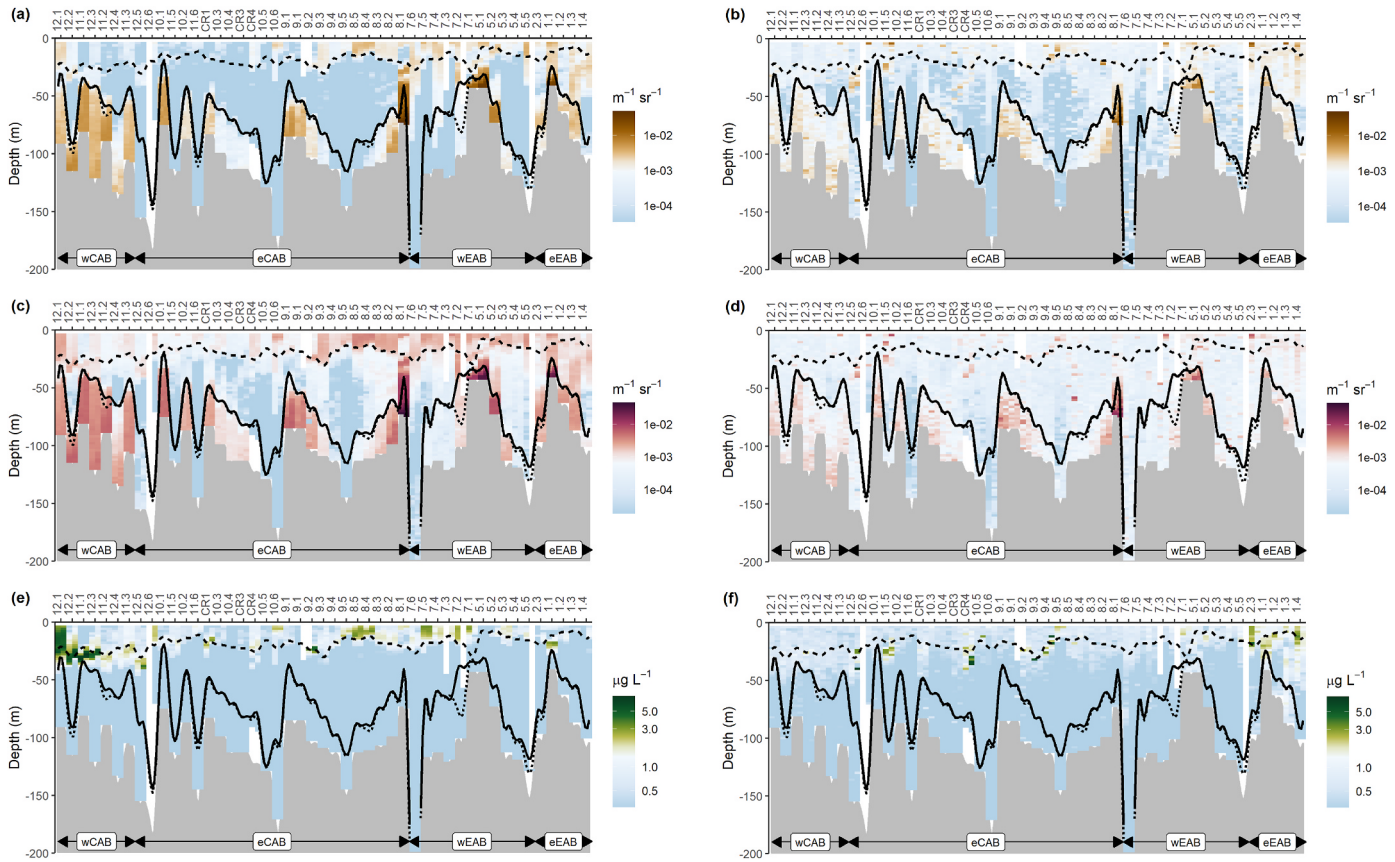

Fig. 2. Particle assemblages for small particles ("baseline") and large particles ("spikes") as identified using optical backscattering at **(a, b)** 532 nm (top row), **(c, d)** 700 nm (middle row), and **(e, f)** Chlorophyll-*a* fluorescence (bottom row). Stations are sorted from west to east, with the station name (*TT.S*) indicating the transect (*TT*) and inshore-offshore position (*S*, with 1 being closest to the shore). The geographical sections (wCAB, eCAB, wEAB and eEAB) are indicated by the horizontal lines. Grey polygon shows bathymetry. Upper and lower dark lines indicate the limit of the surface mixed layer (dashed line) and bottom mixed layer defined by a 0.01 or 0.02 kg m^{-3} difference in density from the deepest density (dotted and solid lines, respectively).

$$b_{bp} = b_{bp\_baseline} + b_{bp\_spikes} = b_{bp\_small} + b_{bp\_large} \quad (1)$$

where b_{bp_small} are small particles *and* b_{bp_large} are large particles. For this method, large particles are considered to be approximately ≳100 µm in diameter (Briggs et al., 2020). This method is a bulk method and it cannot detect whether multiple large particles are passing through the sampling volume at the same time. Particulate backscattering values below zero (negative values) indicated that particle concentrations were below the instrument's detection limit, and these values were set to zero. Small particles were defined as the baseline signal calculated using a running minimum filter (11-point; Briggs et al., 2020) while large particles were defined as the spikes and calculated as the difference between the recorded signal and the baseline signal (Eq. (1)).

The descent/ascent speed of the platform affects spike height. To minimize this effect, we calculated the platform speed over 24 readings (i.e., 2.4 s) and on changes in depth. Only recordings taken at a descent/ascent speed between 0.2 and 1.0 m s^{-1} were considered in further analyses (53% of the data met these criteria). Furthermore, we excluded shallow samples (<4 m depth) as spikes near the surface are likely to include bubbles from waves, the sensor platform entering the water, and ship movement.

At the end of this processing, six variables were obtained: two signals were calculated (baseline and spikes) for each backscatter wavelength (532 and 700 nm) and Chl fluorescence, which were then averaged into 2-m bins for the downcast and upcast at each station.

2.4. Clustering approach and analysis of spatial trends

We explored spatial patterns of particle assemblages using hierarchical cluster analyses in R (3.5.1) (R Core Team, 2018). We tried a variety of clustering approaches and used different bin sizes, standardizations and transformations. The results were all consistent with the data interpretation in this paper, indicating that our method was robust. First, baseline and spike values for 532 nm, 700 nm and Chl fluorescence were scaled to have a mean of 0 and a standard deviation of 1. We calculated Euclidian distances and performed hierarchical clustering (average linkage method; cophenetic distance: 0.96) to look at the overall data structure. The first few branches were dominated by very few observations, indicative of outliers that cause issues with the initial cluster analysis. To identify and separate these outliers, we increased the number of initial clusters from 2 to 60 and recorded the number of observations in each initial cluster, with the largest initial cluster being defined as the 'core' group. Typically, the incremental increase in the number of initial clusters did not increase the number of observations outside the core group, indicating that the additional cluster contained observations that were already outside the core group. With the addition of the 35th cluster, 266 observations were cleaved from the core group, which we took as indication that we are tapping into the core group. We therefore applied 34 clusters, defined the largest cluster as 'core' data, and grouped the remaining clusters as 'outlier' data. The outlier group contained 155 observations (4% of the data). Once observations were assigned to one of the groups (core or outlier), both groups were individually scaled (from raw data) to have a mean of 0 and a standard deviation of 1.

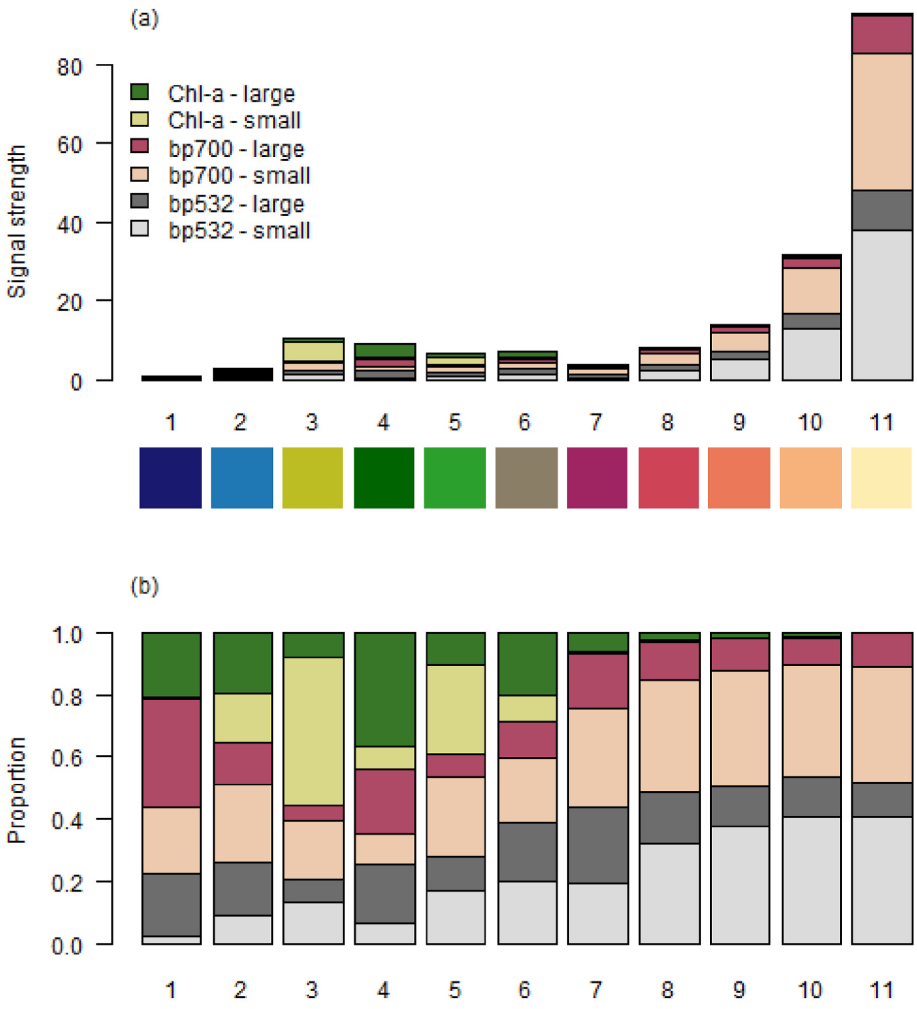

Fig. 3. Mean cluster composition. (a) Total signal strength of 532 nm, 700 nm (both in $\times 10^{-3}$ m^{-1} sr^{-1}) and Chl fluorescence (in µg Chl L^{-1}) in baseline and spike signals (small and large particles, respectively). (b) Relative contribution of each to total signal strength. Bar colours in grey, red and green show 532 nm ('bp532'), 700 nm ('bp700') and Chl fluorescence ('Chl-a'), respectively. Lighter colours represent baseline signal ("small"), darker colours represent spike signal ("large"). The coloured squares underneath each bar relate the clusters with the colour legend used in Figs. 4–6. The cluster numbering (1–11) is shown at the bottom of the figure.

Using the two groups identified in the previous analysis (core and outlier), we further partitioned them using a k-means clustering, resulting in 7 and 4 clusters in the core and outlier data, respectively. The optimal number of clusters was determined using R's *NbClust* function in the *NbClust* package (Charrad et al., 2014). The clusters within each group were visualized on principal component maps (using the *fviz_cluster* function from R's *factoextra* package) (Supplementary Fig. 1).

To explore the spatial trends in the composition of profiles, we produced an abundance table of the clusters for each station and analysed these using multivariate ordination (non-metric multidimensional scaling (NMDS) using the *vegan* package in R; Oksanen et al., 2016). The data were square-root transformed and standardized (Wisconsin double standardization) to reduce the influence of clusters with high abundance. Bray-Curtis dissimilarities were calculated (*metaMDS* function) with an acceptable level of stress (0.2; Legendre and Legendre, 1998). The solution was centred, rotated so that the first axis expresses the largest variance, and scaled so that a distance of one unit between two profiles indicates a halving of profile similarity. The first axis approximated water column depth ($p < 0.001$, $R^2 = 0.43$) as determined using the *envfit* function, which fits environmental vectors onto the ordination. The solution was hence rotated (*MDSrotate* function) so that the first axis is parallel to water column depth.

We tested for significant differences (1) between inshore and offshore stations (defined as the two first and last stations on each transect, respectively; Fig. 1), (2) between the four sections (wCAB, eCAB, wEAB and eEAB), and (3) between stations with and without near-bottom turbidity. The difference between these different groups (*a priori* groups) was tested using PERMANOVA (non-parametric multivariate analysis of variance; Anderson, 2001) via the *adonis* function after applying the same transformation and dissimilarity calculations (*vegdist* function) as described above. Differences in dispersion, which can give false positives (Anderson, 2006), were tested using the *betadisper* and *permutes* functions. Dispersion was not significantly different between any of the pairings ($p \geq 0.10$ in all cases).

3. Results

3.1. Signal strengths

Generally, there was a strong correlation between the baselines of the two backscattering wavelengths (linear regression: $p < 0.001$, $R^2 = 0.93$, $n = 3850$), as well as for the spikes detected by these two sensors (linear regression: $p < 0.001$, $R^2 = 0.51$, $n = 3850$). Chl fluorescence baseline and spikes did not correlate with each other nor with any of the other sensor outputs.

In terms of raw signals, the baselines of 532 and 700 nm backscatter were highest near the sea-bed (Fig. 2a, c), with their spikes following a similar pattern with higher signal strength also near the seabed (Fig. 2b, d). Baseline Chl fluorescence and Chl fluorescence spikes were strongest in the surface mixed layer (Fig. 2e and f). On a spatial scale, all three sensors detected higher concentrations throughout the water column on the most eastern transects (transects 1 and 2; Fig. 2).

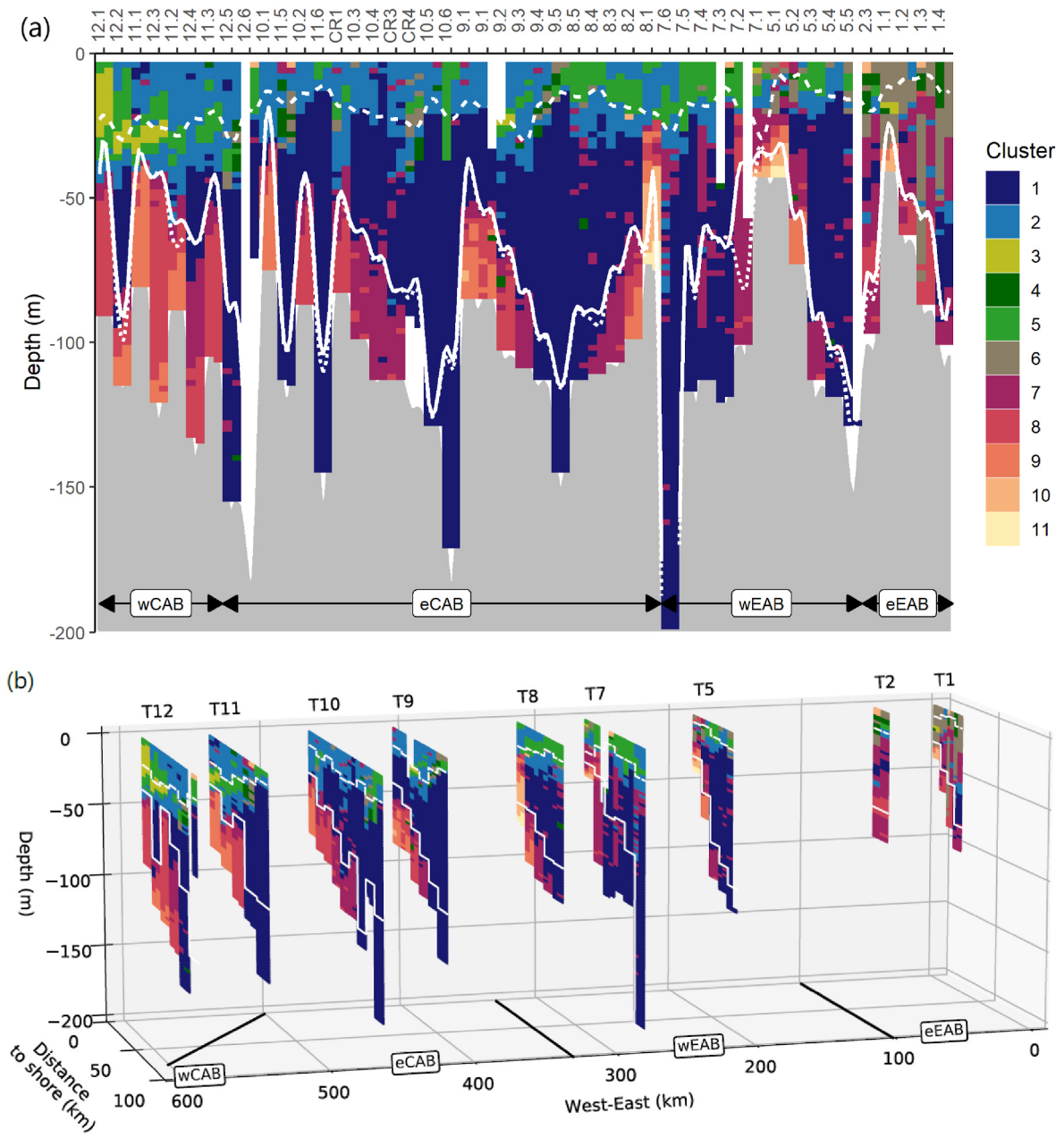

Fig. 4. Vertical distribution of particle clusters over the Agulhas Bank in March 2019. The geographical sections (wCAB, eCAB, wEAB and eEAB) are indicated by the horizontal lines. Upper and lower white lines indicate the limit of the surface mixed layer (dashed line) and bottom mixed layer defined by a 0.02 kg m^{-3} difference in density from the deepest density (solid line). **(a)** Stations are sorted from east to west, with the station name (*TT.S*) indicating the transect (*TT*) and inshore-offshore position (*S*, with 1 being closest to the shore). Grey polygon shows bathymetry. Dotted line shows bottom mixed layer as defined by 0.01 kg m^{-3} difference in density from the deepest density. **(b)** 3D representation of clusters. T1 to T12 correspond to the transect numbers.

3.2. Particle assemblages

Using the k-means clustering, we detected 11 distinct particle assemblage clusters (Fig. 3), with the seven core clusters encompassing 96% of the observations, the four clusters classified as outlier clusters (clusters 3*, 4*, 10* and 11*, indicated by asterisks thereafter) encompassing the remaining 4% of the observations (Supplementary Fig. 1).

We identified the following trends and colour-coded the clusters accordingly (Fig. 3). Clusters 1 and 2 (blue colours) were lowest in particle concentrations of backscattering at 532 nm (means of 0.2×10^{-3} and 0.8×10^{-3} m^{-1} sr^{-1}, respectively) and 700 nm (means of 0.5×10^{-3} and 1.2×10^{-3} m^{-1} sr^{-1}), and Chl fluorescence (means of 0.2 and 1.1 μg Chl L^{-1}). Cluster 1 (lowest particle concentrations; dark blue) dominated the mid-water column at most of the deeper offshore stations. At shallower stations, Cluster 1 was restricted to the mid-water column. Cluster 2 (light blue; with slightly more elevated particle concentrations than Cluster 1) was prevalent in, and just below, the surface mixed layer except on transect 1, where other clusters dominated near the surface (Fig. 4).

Clusters 3 to 6 (green colours) were similar in particle concentration (means on average 2.3×10^{-3} m^{-1} sr^{-1}, 2.4×10^{-3} m^{-1} sr^{-1} and 3.6 μg L^{-1} for 532 nm, 700 nm and Chl fluorescence, respectively), but varied markedly in composition (Fig. 3). Cluster 3* (light green) was richest in baseline Chl fluorescence (4.9 μg Chl L^{-1}), whereas cluster 4* (dark green) was richest in Chl fluorescence spikes (3.3 μg Chl L^{-1}). Cluster 5 (mid-green) appeared similar to Cluster 3*, though with less baseline Chl fluorescence (1.9 vs 3.9 μg Chl L^{-1}, respectively). Cluster 6 (khaki) appeared enriched in spikes (particularly Chl fluorescence spikes; 1.5 μg

Table 2
Typical signal strength (mean and standard deviation) of optical backscattering (532 nm and 700 nm in $\times 10^{-3}$ m^{-1} sr^{-1}) and Chl fluorescence (in µg Chl L^{-1}) for each cluster. Average depth as well as closest distance to the surface and the seabed[a] where each cluster was found and number of observations in each cluster are also presented. * indicate 'outlier' clusters.

Cluster	Observations	Depth (m)				532 nm ($\times 10^{-3}$ m^{-1} sr^{-1})				700 nm ($\times 10^{-3}$ m^{-1} sr^{-1})				Fluorescence (µg Chl L^{-1})			
		mean	SD	Min. dist. surface[a]	Min. dist. seabed[a]	baseline		spike		baseline		spike		baseline		spike	
						mean	SD	mean	SD	mean	SD	mean	SD	mean	SD	mean	SD
1	1806	80	53	26	8	0.0	0.1	0.2	0.2	0.2	0.2	0.3	0.2	0.0	0.0	0.2	0.1
2	577	21	16	4	45	0.3	0.5	0.5	0.3	0.8	0.5	0.4	0.2	0.5	0.3	0.6	0.1
3*	46	22	8	8	29	1.4	0.7	0.8	0.4	1.9	0.5	0.5	0.4	4.9	1.1	0.9	0.6
4*	54	29	26	6	23	0.6	0.7	1.7	1.4	0.9	0.7	1.9	1.4	0.7	0.9	3.3	4.1
5	225	16	9	4	52	1.1	0.9	0.7	0.4	1.7	0.9	0.5	0.2	1.9	0.6	0.7	0.2
6	148	21	14	4	18	1.5	0.9	1.3	0.5	1.5	0.6	0.9	0.3	0.6	0.6	1.5	0.4
7	568	67	29	22	4	0.7	0.6	0.9	0.5	1.2	0.6	0.7	0.3	0.0	0.1	0.3	0.2
8	351	75	23	36	3	2.6	0.8	1.3	0.5	2.9	0.7	1.0	0.4	0.0	0.0	0.2	0.2
9	175	71	22	33	0	5.3	1.2	1.8	0.6	5.2	0.9	1.4	0.5	0.0	0.0	0.3	0.2
10*	44	42	18	4	4	12.9	7.4	4.1	3.0	11.2	5.9	2.8	1.6	0.1	0.4	0.6	0.5
11*	11	60	15	40	0	38.1	6.0	9.8	3.3	34.6	7.1	9.7	4.5	0.0	0.1	0.5	0.2

[a] To calculate the closest distance to surface or seabed, the depth data for each cluster were sorted in an ascending order and the first 5% of the data were ignored to remove the effect of potential outliers.

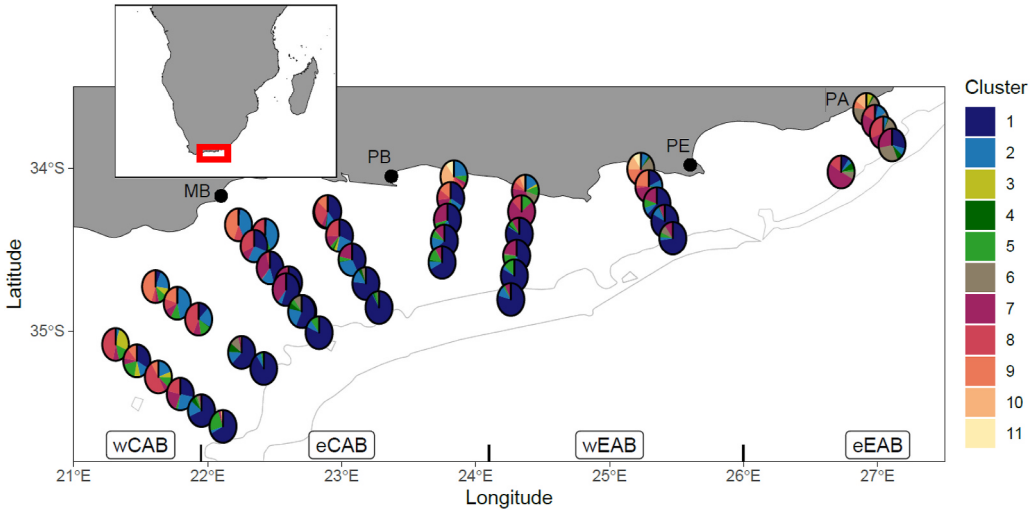

Fig. 5. Spatial distribution of clusters. Pies show relative occurrence of clusters at each site (combined up- and downcast). Colours are as in Fig. 3. The geographical locations (wCAB, eCAB, wEAB and eEAB) are indicated. The 200 m and 1000 m isobaths (grey lines) indicate approximately the edge of the shelf. (PA: Port Alfred, PE: Port Elizabeth (now Gqeberha), PB: Plettenberg Bay, MB: Mossel Bay).

Chl L^{-1}) and, within this cluster group, was most similar to clusters 7–11* in terms of relative signal composition (Fig. 3b). This cluster group (3*-6) was observed predominantly near the surface and around the base of the surface mixed layer, except Cluster 6, which was predominantly located on transect 1 and 2 at variable depths (Fig. 4).

Clusters 7 to 11* (reddish colours) increased progressively in 532 and 700 nm backscatter signals (both baseline and spike; from 1.7×10^{-3} to 47.9×10^{-3} and 1.9×10^{-3} to 44.3×10^{-3} m^{-1} sr^{-1}, respectively), whereas Chl fluorescence signals (both baseline and spikes) were at a low intensity (from 0.2 to 0.7 µg Chl L^{-1}). These clusters (7–11*) were confined to near the seabed in the bottom mixed layer (Fig. 4).

The threshold value for high near-bottom turbidity was determined, using visual inspection of all profiles for a marked increase of the backscatter signal (700 nm) towards the seabed (Townsend et al., 1992), as $>13 \times 10^{-3}$ m^{-1} sr^{-1}. This threshold value corresponded to ~1.2 Nephelometric Turbidity Units (NTU), and to clusters 10* and 11* (Table 2).

3.3. Spatial trends and benthic nepheloid layer (BNL)

Inshore and offshore stations were significantly different in their particle composition ($p = 0.001$, PERMANOVA; Fig. 6b). Low particle concentrations dominated the water columns near the shelf break while, towards the coast, clusters with higher 532 and 700 nm backscatter intensity (reddish colours) started to be more prevalent (Figs. 4 and 5). High-concentration clusters (clusters 10* and 11* in pale orange and yellow) were found near the seabed and at the shallow stations on the eastern CAB and the EAB (Stations 1.1, 5.1, 7.1, 8.1 and 9.1).

Stations in middle sections of the study area (eCAB and wEAB) were not significantly different ($p = 0.21$, PERMANOVA), with a clear overlap on the ordination plot (Fig. 6c). The western and eastern parts of the CAB, however, were significantly different ($p = 0.001$, PERMANOVA). Likewise, the western and eastern parts of the EAB were significantly different ($p = 0.008$; PERMANOVA). Most distinct were the two most distance sections, wCAB and eEAB ($p = 0.001$, PERMANOVA) with a clear separation in the ordination plot (Fig. 6c).

Finally, we identified stations with a BNL, based on a sharp increase in backscatter signal near the seabed and exceeding the BNL threshold ($>13 \times 10^{-3}$ m^{-1} sr^{-1}; ~1.2 NTU), as Stations 1.1, 5.1, 7.1, and 8.1. All four BNL stations were the most inshore stations and had significantly different particle compositions compared to the remaining stations ($p = 0.001$; PERMANOVA; Fig. 6d).

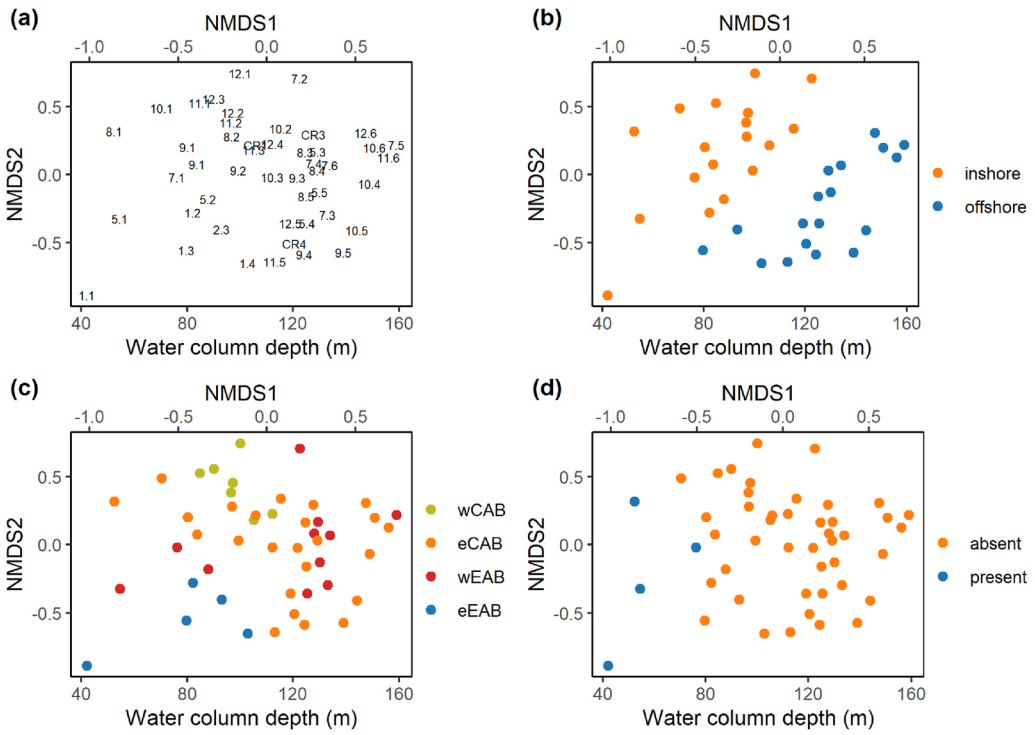

Fig. 6. Particle profiles in the sampling region were evaluated using non-metric multidimensional scaling (NMDS). The distance between points represents the degree of similarity (or dissimilarity) between the composition of the assemblages of particle profiles (i.e., stations closer together are more similar). The horizontal axis approximates the water column depths at the profile locations. The scatter plots identify (a) profiles, (b) relative position along each transect, with the two first and last stations on each transect defined as "inshore" (orange) and "offshore" (blue), respectively, (c) sections (wCAB, eCAB, wEAB and eEAB in green, orange, red and blue, respectively), and (d) whether a benthic nepheloid layer (BNL) was present (blue) or not (orange).

4. Discussion

Our relatively simple, semi-supervised cluster analysis identified 11 different particle assemblage types that allow insights into the Agulhas Bank ecosystem dynamics. We observed a clear inshore-offshore trend in particle assemblages (Figs. 4–6), as well as different regions along the Bank with the eEAB, wEAB + eCAB and wCAB being different in their vertical particle compositions (Figs. 6 and 7). In the following discussion, we will explore how the spatial trends in particle composition on the EAB and CAB are linked to environmental parameters. We will further consider the formation of high near-bottom turbidity.

4.1. Large aggregate formation off Port Alfred

The characteristics of the particle assemblages near Port Alfred in the eEAB was distinctly different to those in the other sections (Fig. 7), suggesting different biophysical dynamics near Port Alfred. The region near Port Alfred is well known for its frequent coastal wind-driven upwelling during easterly wind events, which brings bottom waters of Indian Ocean Central Water origin to the surface (Lutjeharms et al., 2000; Whittle et al., 2008). Typically associated with this upwelling is the introduction of inorganic nutrients that leads to high primary production in near coastal waters (Lutjeharms et al., 2000; Mazwane et al., this issue). We observed that the water column near Port Alfred was high in Chl fluorescence (Clusters 3–6), in particular Chl fluorescence spikes (Fig. 2f; Clusters 4 and 6 in Figs. 4 and 5), indicating high Chl concentrations and a high abundance of large Chl-rich aggregates or phytoplankton. During our study, measured Chl concentrations were high while net primary production was relatively low in the east around Port Alfred (Station 1.1: 106 mg Chl m^{-2} and 0.3 g C m^{-2} d^{-1}; Poulton et al., this issue). We interpret these conditions as the end of an upwelling event when nitrate has become limiting by the time we sampled (<0.2 μM NO_x in the surface mixed layer; Poulton et al., this issue). The upwelled nutrients may have initially caused the growth and accumulation of phytoplankton cells, particularly microplankton including diatoms. Microplankton were common in this region during our study (66 ± 25% of total Chl in the surface mixed layer in the eEAB compared to 25 ± 19% across all other stations; Poulton et al., this issue), contrasting the western stations where picoplankton became relatively more important (30 ± 16% of total Chl in the surface mixed layer compared to 11 ± 16% in the eEAB; Poulton et al., this issue). The high biomass of large-celled phytoplankton in the eEAB could have led to the formation of large phytodetritus aggregates, which would explain the Chl fluorescence spikes observed here. Hence, the distinct upwelling regime and resulting phytoplankton community can explain the markedly different optical particle composition (high occurrence of both backscatter and Chl fluorescence spikes) in the eEAB section when compared to the wEAB and CAB (Fig. 2).

The presence of optical spikes below the mixed layer in the open ocean has been interpreted as sinking phytodetritus aggregates (Briggs et al., 2011), i.e., indicating a vertical transfer of surface organic matter to depth. As the eEAB had the highest abundance of spikes (compared to other sections), we would expect sinking particulate fluxes to be highest here. Particle flux measurements carried out during the cruise, using the Marine Snow Catcher, confirm that particle fluxes were highest near Port Alfred (1.9 g C m^{-2} d^{-1} at 20 m depth at Station 1.4 compared to, on average, 0.7 ± 0.3 g C m^{-2} d^{-1} in the upper 40 m across all other stations; Malongweni et al., 2022). The relatively high biogenic silica fluxes here (60 mg bSi m^{-2} d^{-1} compared to, on average, 9 ± 9 mg bSi m^{-2} d^{-1} in the upper 40 m across all other stations; Malongweni et al., 2022) further supports the hypothesis that diatoms were an important component in the phytoplankton community and led to the formation of sinking aggregates. Overall, the region near Port Alfred may be a region of high vertical transport of organic matter to depth via sinking particles (Malongweni et al., 2022).

4.2. Bottom turbidity and benthic nepheloid layer (BNL) formation

Across the study region, we consistently observed elevated particle concentrations near the seabed at the shallower inshore stations, indicating a persistent potential for high turbidity events and BNL formation on the Agulhas Bank. This observation is consistent with the suggested BNL intensity in this region (Gardner et al., 2018). The key question is whether these high particle concentrations are caused by sinking matter

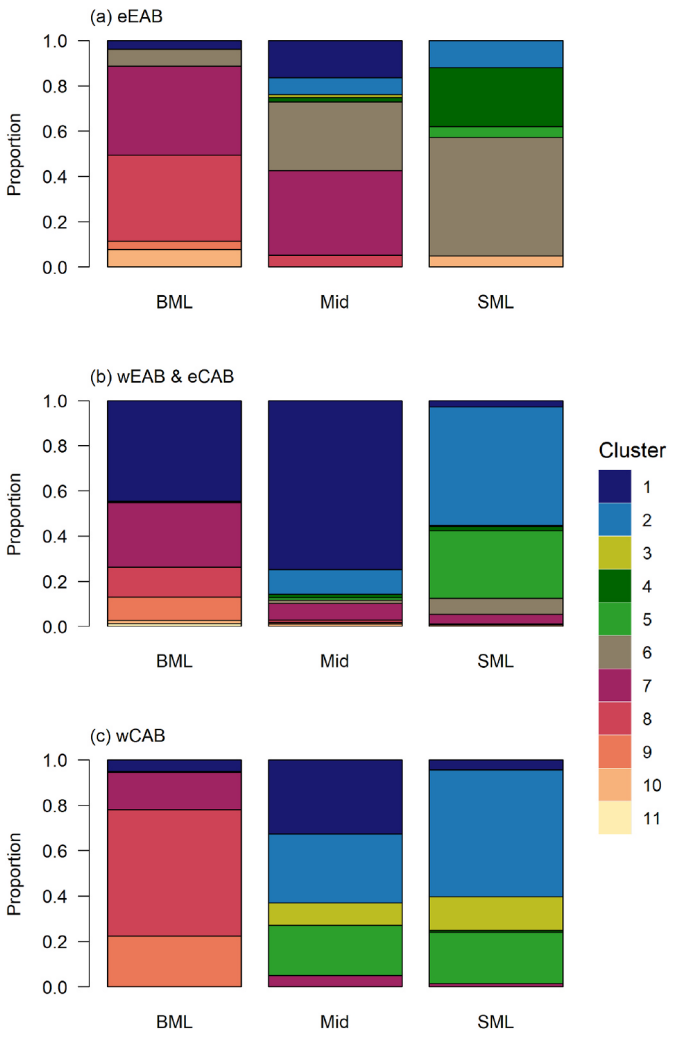

Fig. 7. Optical characteristics in the (a) eEAB, (b) wEAB and eCAB, and (c) wCAB for the bottom mixed layer (BML), midwater column ('mid') and surface mixed layer (SML). Colours show clusters as in legend.

(e.g. marine snow) accumulating above the seabed, by resuspension of seabed sediments, or a combination of both. Advection of sediments from offshore via the Agulhas Current cannot explain high turbidity as the offshore waters were clearer than inshore waters (Fig. 4).

4.2.1. *Accumulation of sinking organic matter*

If the formation of BNLs was directly linked to sinking marine snow and the system was at steady state, we would expect to observe elevated particle concentrations near the seabed around the same time as a high abundance of Chl fluorescence spikes in the overlying water column. These spikes are indicative of large, sinking phytodetritus aggregates that could accumulate near the seabed and cause low visibility. During our study, BNLs (here defined as >1.2 NTU) were only observed at the inshore stations on transects 1, 5, 7 and 8. The vertical profiles of the particle composition at these four sites (Fig. 8a) revealed that these sites differed markedly from each other in their Chl fluorescence signals and generally did not have a high abundance of Chl fluorescence spikes (overall few 'green' clusters; Fig. 8a). Moreover, across these four stations, Station 8.1 showed the most pronounced BNL (the highest turbidity at >3 NTU) yet appeared to have the lowest occurrence of Chl fluorescence spikes (Fig. 2f). Our data hence suggest that there is no instantaneous link between the presence of BNL and the particle assemblages in the water column directly above.

Another strong indication that there is no instantaneous link between BNL and sinking "fresh" phytodetritus is provided by the comparison of the depth profiles of Chl fluorescence and red backscatter signal at the four 'BNL sites' (Fig. 8b and c). The vertical profiles show that Chl fluorescence (indicative of phytoplankton and "fresh" phytodetritus) was not notably enriched near the seabed, whereas the red backscatter intensity (indicative of suspended matter) increased greatly near the seabed. Moreover, the vertical Chl fluorescence profiles varied considerably between the four stations, suggesting different biophysical dynamics at these sites. In other words, the presence of BNL appeared to be decoupled from the concurrent phytoplankton dynamics above.

As our observations are a 'snapshot' in time, we cannot rule out that there was a time lag in phytodetritus export and BNL formation. For the open ocean, non-steady state conditions can result in a misinterpretation of flux profiles and particle export dynamics when export changes over timescales of similar magnitudes to particle sinking velocities (Giering et al., 2017). At typical sinking velocities of 20–100 m d^{-1} (Villa-Alfageme et al., 2016), exported matter would reach the bottom mixed layer of the Agulhas Bank within a few days (from less than a day to around a week). The residence time of organic matter (i.e., how long we may expect to find elevated particle concentrations in the bottom mixed layer) then depends on the remineralization (i.e., degradation) rate. At a temperature of 8–12 °C (observed range), we expect pelagic remineralization rates of 0.05–0.08 d^{-1} (calculation based on Eq. 7 by Giering et al. (2017) and Iversen and Ploug (2013), implying that ~50% of the organic matter would be remineralized within 8–14 days. Benthic remineralization rates are potentially higher than these estimated rates; nonetheless, a BNL originating from a large export event could persist for several days and be shifted by the tides and bottom currents, even after upper water column plankton dynamics (production, fluxes) have returned to base levels. It is hence possible that the material that makes up BNL partly originates from sinking phytodetritus, with the time lag between export events and benthic remineralization obscuring a direct link between surface productivity and BNL.

4.2.2. *Inshore-offshore trends in turbidity*

We observed a strong correlation between particle concentrations within 5 m above the seabed and water column depth (Fig. 9) that can effectively be interpreted as an inshore-offshore gradient of near-bottom turbidity across the shelf. A possible explanation for this trend is an equivalent gradient in primary production and subsequent export, with higher rates towards coastal waters, hence an increased potential for organic matter accumulation inshore. During our survey, as well as over a 20-year remote sensing time series, we indeed observed such inshore-offshore trends in primary production (>650 g C m^{-2} y^{-1} near the coast and <550 g C m^{-2} y^{-1} above the 200 m isobath based on satellite-derived average annual net primary production between 1998 and 2018; Mazwane et al., this issue) and export fluxes (derived using Marine Snow Catchers: ~950 mg C m^{-2} d^{-1} near the coast and 460 mg C m^{-2} d^{-1} near the 200 m isobath; Malongweni et al., 2022).

An alternative explanation for the observed inshore-offshore gradient in turbidity could be a consistent pattern in the resuspension of sediments. Current flow along the shelf edge is generally aligned with the Agulhas Current, with a strong westward flow, whereas on the central Agulhas Bank the current is weaker and, at times, reversed close to the shore (Boyd et al., 1992). This decrease in current flow towards the coast is supported by the mooring transect near Mossel Bay that we recovered during our cruise (Hancke et al., this issue). According to this 6-month time series, tidal speeds and mean residual currents were slower near the coast (mean flow of 7 cm s^{-1} throughout the water column at inshore station CR1) than near the shelf edge (15 and 13 cm s^{-1} at offshore stations CR3 and CR4, respectively; Hancke et al., this issue). Yet, at all sites, maximum velocities of >30 cm s^{-1} were recorded. Moreover, coastal trapped waves and internal solitary waves, which have been shown to induce nepheloid layers (Boegman and Stastna, 2019; McCave, 2009; Tian et al., 2019, 2021a, 2021b), have been recorded in this region (Jackson, 2004; Schumann and Brink, 1990;

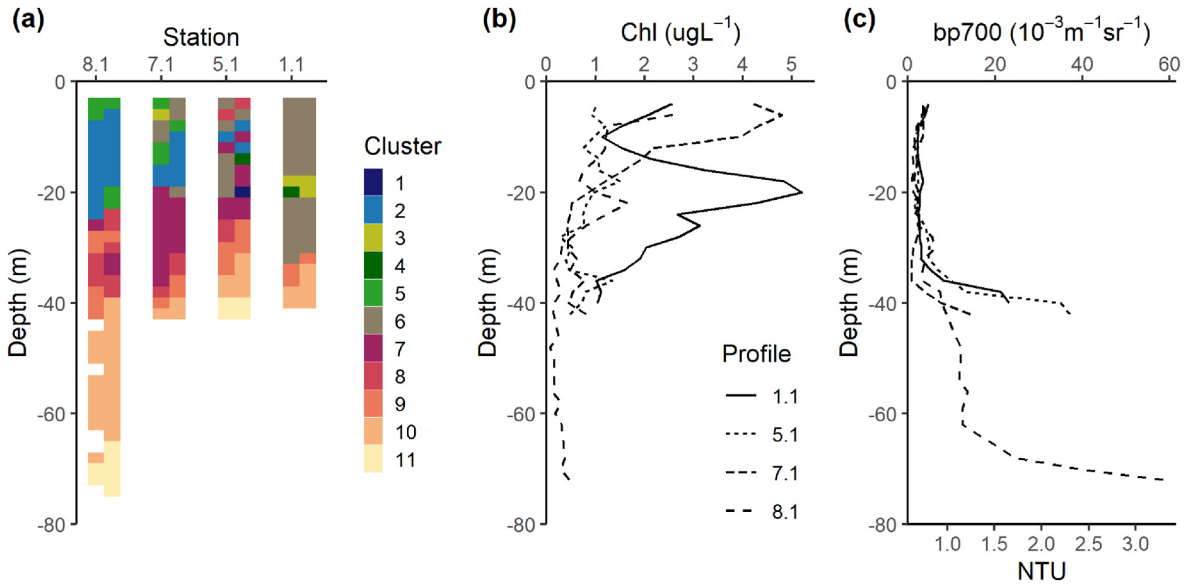

Fig. 8. Profiles where BNLs were observed (1.1, 5.1, 7.1 and 8.1). (a) Vertical distribution of particle clusters at the stations. (b) Depth profiles of Chlorophyll-*a* fluorescence (in μg L^{-1}) and (c) backscatter strength (sum of small and large particles at 700 nm in 10^{-3} m^{-1} sr^{-1}). Line type indicates profile as shown in legend. Corresponding NTUs are also shown.

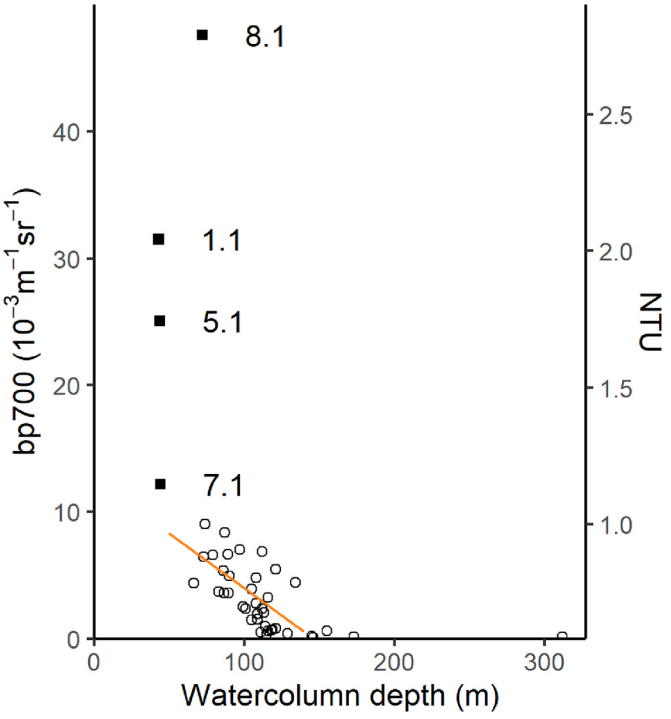

Fig. 9. Correlation between backscatter strength (mean of bp700 in 10^{-3} m^{-1}sr^{-1} 5 m above the seabed) and water column depth (in m). Solid squares show high concentrations at station 1.1, 5.1, 7.1 and 8.1. Orange line shows linear regression of all stations except the deep station (>300 m) and stations 1.1, 5.1 and 8.1 ($p < 0.001$, $R^2 = 0.54$, $n = 39$). Corresponding NTUs are also shown.

Hancke et al. this issue).

Limited information is available on the benthic habitat and substrate type, particularly sediment size, across the Agulhas Bank (Sink et al., 2012; Wilkinson and Japp, 2005). Most of the CAB and EAB are covered with biogenic sandy sediments, and muddy substrates are found in isolated patches towards the coast (<100 m depth) typically near estuaries (Sink et al., 2012; Wilkinson and Japp, 2005). The sediments near the coast are likely finer than those towards the shelf break (Sink et al., 2012; Wilkinson and Japp, 2005), and this region is hence likely more susceptible to resuspension. It is thus possible that the result is an inshore-offshore gradient in turbidity, as observed here. In addition, due to Ekman veering along the shelf break, clear and cold waters are being pushed along the seabed towards the coast (Hutchings 1994). Such intrusions could also explain the clearer near-bottom waters towards the shelf edge. We suspect that a combination of all of the above contributes to the observed cross-shelf turbidity pattern. There is a clear need for future research, including dedicated experiments (e.g. Thompson et al., 2019), surveys of benthic habitats and substrate as well as near-bottom shear stress across the Agulhas Bank.

4.3. Particle retention and remineralization on the CAB

Boyd and Shillington (1994) showed the presence of a retention cell on the CAB and suggested that this cell was caused by the divergent flows of the Agulhas Current on the outer shelf, which flows westward, and the wind-driven coastal current, which flows eastwards. Though there was considerable variability in the exact position and feature strength of the retention cell, it was persistently found over a period of four years (1988–1991), located offshore between Still Bay and Mossel Bay, at approximately 35°S 21.5°E. Partly based on that study, Hutchings (1994) suggested that a larger cyclonic recirculation pattern dominates the CAB (between Still Bay ~21°E and Plettenberg ~23.5°E) during summer, which would restrict offshore losses. The retention of particles in this region was later backed by a particle-tracking model used to investigate the transport and retention of sardines (Miller et al., 2006).

The inshore stations of our transects 11 and 12 were located at the site of this suggested retention cell. The vertical profiles in this section (wCAB) differed from those in the other sections in a number of characteristics. The surface mixed layer tended to be deeper and stratification stronger (based on maximum buoyancy frequency). Noticeable were also a sub-surface Chl maximum just below the surface mixed layer and a clear enrichment with non-fluorescent particles near the seabed (Figs. 4 and 5; Poulton et al., this issue), as well as higher zooplankton densities (Noyon et al., 2022).

If a persistent cyclonic circulation would indeed retain the biota in the mid-bank region, we could expect to find corresponding ecosystem

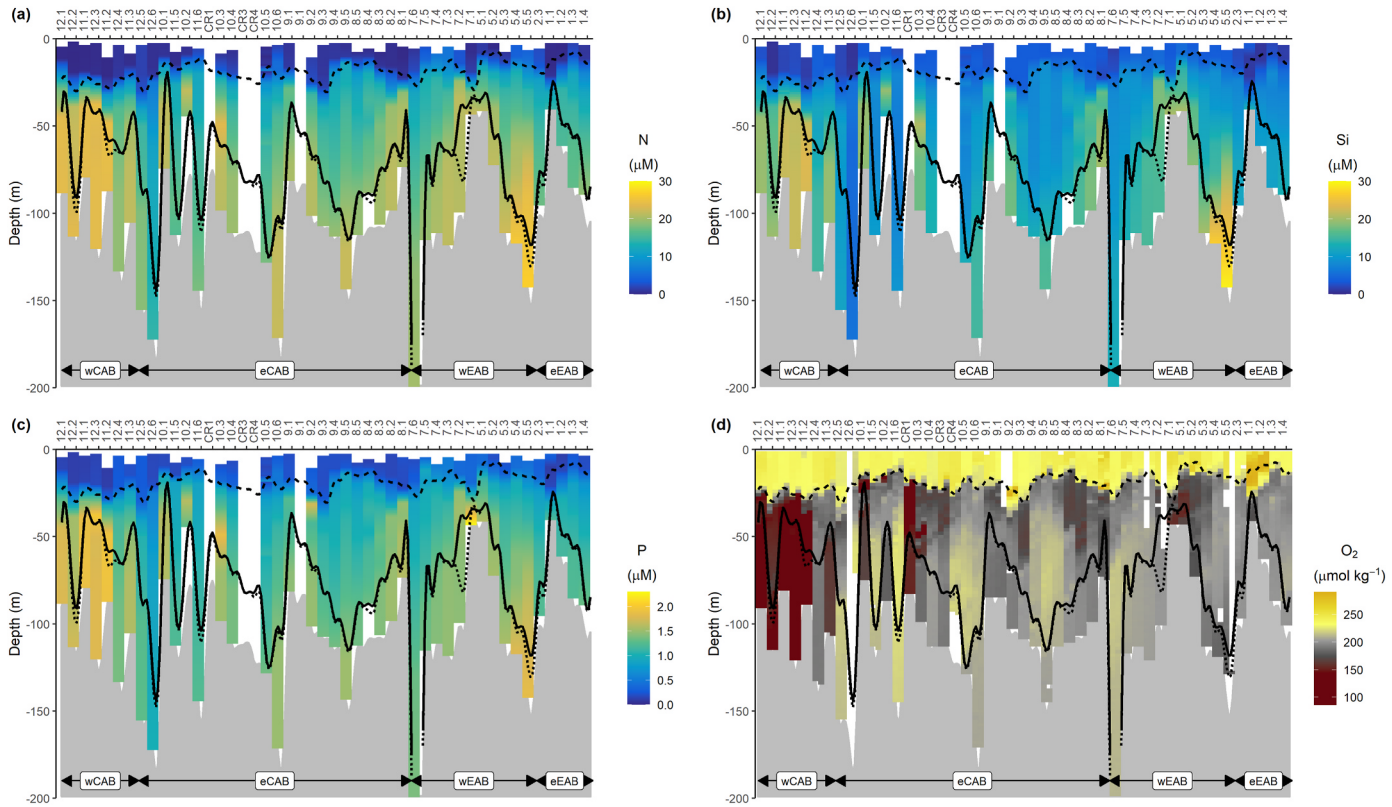

Fig. 10. Nutrient concentrations during the survey. (a) Nitrate + nitrite (range: 0–30 μM), (b) silicate (range: 0–30 μM), (c) phosphate (range: 0–2.3 μM), and (d) oxygen (85–290 μmol kg^{-1}). Concentrations are as indicated in colour bars. Stations are sorted from west to east, with the station name (*TT.S*) indicating the transect (*TT*) and inshore-offshore position (*S*, with 1 being closest to the shore). Grey polygon shows bathymetry. Upper and lower dark lines indicate the limit of the surface and bottom mixed layers, respectively. Upper and lower dark lines indicate the limit of the surface mixed layer (dashed line) and bottom mixed layer defined by a 0.01 or 0.02 kg m^{-3} difference in density from the deepest density (dotted and solid lines, respectively).

characteristics. In regards to particle fields, it is unlikely that we would be able to see distinct direct effects on the vertical distribution of our clusters as 'retention' is a temporal phenomenon rather than an instant, short-term one. Hence, we would not necessarily be able to distinguish the retention cell when comparing the similarities in our 'snapshot' vertical particle profiles (e.g., Fig. 6c). Rather, we need to look for signals of processes that integrate over time.

We discussed above (Section 4.2) that two processes likely occurred in the bottom mixed layer across the western and central sections of our study site: the remineralization of accumulated sinking organic matter, and resuspension. Remineralization, i.e., the conversion of organic matter into inorganic carbon and nutrients, typically requires the consumption of oxygen. Hence, in a closed system, regions of high or prolonged remineralization rates can be identified by elevated nutrient concentrations and low oxygen concentrations. At the inshore stations of transects 11 and 12 (wCAB), we indeed observed strong gradient in nutrients (nitrate, silicate and phosphate), with low nutrient concentrations in the surface mixed layer (e.g., 0.1–1 μM N) and high nutrient concentrations in the bottom mixed layer (e.g., 18–26 μM N) (Fig. 10a–c; see also Poulton et al., this issue). We also observed the lowest oxygen concentrations across our study region here (Fig. 10d). If we assume that microbial remineralization rates were broadly consistent across the study site (based on the observed narrow temperature range of 8–12 °C), these strong concentration patterns support the idea of a longer residence time of the waters in the western section of our study area (Boyd and Shillington, 1994; Hutchings, 1994; Miller et al., 2006).

The relatively strong enrichment with non-fluorescent particles throughout the bottom mixed layer in this region suggests that this layer is well mixed and able to redistribute the nutrients towards the nutrient-depleted surface layers. However, the east-west gradient in stratification strength of the surface mixed layer indicates that it would have been harder to mix these nutrients back up into the surface mixed layer in the west than in the east (see also Poulton et al., this issue). Such trapping of nutrients below the mixed layer may explain why we observed a strong sub-surface chlorophyll maximum in transects 11 and 12 (Fig. 4).

We can further tentatively explore the potential residence time of the particles in the wCAB based on the observed oxygen concentrations. We do not have community respiration measurements for our study site, yet we have community respiration estimates measured in the UK Shelf Sea that experienced similar temperatures and primary production rates as the Agulhas Bank during our study (9–11 °C vs 8–12 °C and median 563 mg C m^{-2} d^{-1} vs 370 mg C m^{-2} d^{-1}, respectively; Poulton et al., 2019; Poulton et al., this issue). Based on a mean annual community respiration rate (0.4 ± 0.31 μM d^{-1} ;García-Martín et al., 2019), it would take ~200 days to produce the observed difference between oxygen concentrations in the bottom mixed layer at the offshore station 11.6 (~220 μmol kg^{-1}) and the inshore station 11.2 (140 μmol kg^{-1}). Overall, our observations are consistent with the suggestion of particle retention on the CAB, at least on timescales that allows the observed change in nutrient and oxygen concentrations.

5. Conclusion

Our data analysis method of optical backscatter and fluorescence allowed us to characterize the vertical structure of particles on the Agulhas Bank, particularly showing a strong cross-shelf gradient of near-bottom turbidity. The narrow shelf region near Port Alfred appeared to be a region distinct from the rest of the shelf, characterized by optical spikes that indicate the presence of large phytoplankton and the vertical transport of organic matter. On the Central Agulhas Bank, turbidity was

higher nearer to the coast, likely because of a combination of increased organic matter accumulation, finer substrate near the coast that is readily resuspended, and the intrusion of clearer offshore waters at the shelf edge near the bottom. Our data further support previous suggestions of particle retention owing to a larger recirculation pattern on the Central Agulhas Bank.

Data availability

Data for fluorescence and backscatter vertical profiles are available under UK Open Government Licence (https://doi.org/10.5285/d9567f7a-ba96-683a-e053-6c86abc0ab7e).

Author statement

Sarah L. C. Giering: Conceptualization, Methodology, Investigation, Validation, Visualization, Writing - Original Draft, Review & Editing, **Margaux Noyon:** Investigation, Validation, Writing - Original Draft, Review & Editing, Project administration, **Brian Godfrey:** Investigation, **Alex J Poulton:** Investigation, **Filipa Carvalho:** Formal analysis, Methodology, **Mike Roberts:** Funding acquisition, Project administration.

Declaration of competing interest

The authors declare that they have no known competing financial interests or personal relationships that could have appeared to influence the work reported in this paper.

Acknowledgements

We thank the captain and crew of EK188 as well as the Department of Agriculture, Forestry and Fisheries (now DEFF) for their support. We thank Stephen Woodward for his support during the survey and Nathan Briggs for advising on the analysis of the backscatter data. We thank all scientists within the SOLSTICE-WIO programme for comments and discussion. Finally, we thank the editors and the four reviewers for their constructive feedback. This publication was produced with the financial support of the Global Challenges Research Fund, UK, in the framework of the SOLSTICE-WIO project (NE/P021050/1). This work is also part of the UK-SA Bilateral Chair in Ocean Science and Marine Food Security by the British Council Newton Fund grant SARCI 1503261 16102/NRF 98399. This publication resulted in part from support from the U.S. National Science Foundation (Grant OCE-1840868) to the Scientific Committee on Oceanic Research (SCOR) and from funds contributed by national SCOR committees.

Appendix A. Supplementary data

Supplementary data to this article can be found online at https://doi.org/10.1016/j.dsr2.2022.105094.

References

Anderson, M.J., 2006. Distance-based tests for homogeneity of multivariate dispersions. Biometrics 62, 245–253. https://doi.org/10.1111/j.1541-0420.2005.00440.x.

Anderson, M.J., 2001. A new method for non-parametric multivariate analysis of variance. Austral Ecol. 26, 32–46. https://doi.org/10.1111/j.1442-9993.2001.01070.

Barbieux, M., Uitz, J., Bricaud, A., Organelli, E., Poteau, A., Schmechtig, C., Gentili, B., Obolensky, G., Leymarie, E., Penkerc'h, C., D'Ortenzio, F., Claustre, H., 2018. Assessing the variability in the relationship between the particulate backscattering coefficient and the chlorophyll a concentration from a global biogeochemical-argo database. J. Geophys. Res. Ocean. 123, 1229–1250. https://doi.org/10.1002/2017JC013030.

Boegman, L., Stastna, M., 2019. Sediment resuspension and transport by internal solitary waves. Annu. Rev. Fluid Mech. 51, 129–154. https://doi.org/10.1146/annurev-fluid-122316-045049.

Boyd, A.J., Taunton-Clark, J., Oberholster, G.P.J., 1992. Spatial features of the near-surface and midwater circulation patterns off western and southern South Africa and their role in the life histories of various commercially fished species. S. Afr. J. Mar. Sci. 12, 189–206. https://doi.org/10.2989/02577619209504702.

Boyd, F.A., Shillington, A.J., 1994. Physical forcing and circulation patterns on the Agulhas Bank. South Afr. J. Sci. 90, 143–154.

Briggs, N., Dall'Olmo, G., Claustre, H., 2020. Major role of particle fragmentation in regulating biological sequestration of CO 2 by the oceans. Science (80-.) 367, 791–793. https://doi.org/10.1126/science.aay1790.

Briggs, N., Perry, M.J., Cetinić, I., Lee, C., D'Asaro, E., Gray, A.M., Rehm, E., 2011. High-resolution observations of aggregate flux during a sub-polar North Atlantic spring bloom. Deep-Sea Res. Part I Oceanogr. Res. Pap. 58, 1031–1039. https://doi.org/10.1016/j.dsr.2011.07.007.

Briggs, N.T., Slade, W.H., Boss, E., Perry, M.J., 2013. Method for estimating mean particle size from high-frequency fluctuations in beam attenuation or scattering measurements. Appl. Opt. 52, 6710. https://doi.org/10.1364/AO.52.006710.

Carter, R.A., McMurray, H.F., Largier, J.L., 1987. Thermocline characteristics and phytoplankton dynamics in Agulhas Bank waters. S. Afr. J. Mar. Sci. 5, 327–336. https://doi.org/10.2989/025776187784522306.

Carvalho, F., Kohut, J., Oliver, M.J., Schofield, O., 2017. Defining the ecologically relevant mixed-layer depth for Antarctica's coastal seas. Geophys. Res. Lett. 44, 338–345. https://doi.org/10.1002/2016GL071205.

Cetinić, I., Perry, M.J., Briggs, N.T., Kallin, E., D'Asaro, E.A., Lee, C.M., 2012. Particulate organic carbon and inherent optical properties during 2008 North Atlantic Bloom Experiment. J. Geophys. Res. Ocean. 117 https://doi.org/10.1029/2011JC007771 n/a-n/a.

Charrad, M., Ghazzali, N., Boiteau, V., Niknafs, A., 2014. NbClust : an R package for determining the relevant number of clusters in a data set. J. Stat. Software 61. https://doi.org/10.18637/jss.v061.i06.

Demarcq, H., Richardson, A., Field, J., 2008. Generalised model of primary production in the southern Benguela upwelling system. Mar. Ecol. Prog. Ser. 354, 59–74. https://doi.org/10.3354/meps07136.

García-Martín, E.E., Daniels, C.J., Davidson, K., Davis, C.E., Mahaffey, C., Mayers, K.M. J., McNeill, S., Poulton, A.J., Purdie, D.A., Tarran, G.A., Robinson, C., 2019. Seasonal changes in plankton respiration and bacterial metabolism in a temperate shelf sea. Prog. Oceanogr. 177, 101884 https://doi.org/10.1016/j.pocean.2017.12.002.

Gardner, W.D., Jo Richardson, M., Mishonov, A.V., Biscaye, P.E., 2018. Global comparison of benthic nepheloid layers based on 52 years of nephelometer and transmissometer measurements. Prog. Oceanogr. 168, 100–111. https://doi.org/10.1016/j.pocean.2018.09.008.

Giering, S.L.C., Sanders, R., Martin, A.P., Henson, S.A., Riley, J.S., Marsay, C.M., Johns, D.G., 2017. Particle flux in the oceans: challenging the steady state assumption. Global Biogeochem. Cycles 31, 159–171. https://doi.org/10.1002/2016GB005424.

Goschen, W.S., Bornman, T.G., Deyzel, S.H.P., Schumann, E.H., 2015. Coastal upwelling on the far eastern Agulhas Bank associated with large meanders in the Agulhas Current. Continent. Shelf Res. 101, 34–46. https://doi.org/10.1016/j.csr.2015.04.004.

Gründlingh, M.L., 1979. Observation of a large meander in the Agulhas current. J. Geophys. Res.: Oceans 84, 3776–3778. https://doi.org/10.1029/JC084iC07p03776.

Hancke, L., Smeed, D., Roberts, M., Rayner, D., Jebri, F., Russo, C., This issue. The structure and dynamics of the cold ridge on the central Agulhas Bank, South Africa . Deep Sea Res. Part II Top. Stud. Oceanogr.

Harris, T.F.W., Legeckis, R., van Forest, D., 1978. Satellite infra-red images in the Agulhas current system. Deep Sea Res. 25, 543–548. https://doi.org/10.1016/0146-6291(78)90642-2.

Hopkins, J.E., Palmer, M.R., Poulton, A.J., Hickman, A.E., Sharples, J., 2021. Control of a phytoplankton bloom by wind-driven vertical mixing and light availability. Limnol. Oceanogr. 66, 1926–1949. https://doi.org/10.1002/lno.11734.

Hutchings, L., 1994. The Agulhas Bank: a synthesis of available information and a brief comparison with other east-coast shelf regions. South Afr. J. Sci. 90, 179–185.

Hutchings, L., Roberts, M.R., Verheye, H.M., 2009. Marine environmental monitoring programmes in South Africa: a review. South Afr. J. Sci. 105, 94–102.

Iversen, M.H., Ploug, H., 2013. Temperature effects on carbon-specific respiration rate and sinking velocity of diatom aggregates – potential implications for deep ocean export processes. Biogeosciences 10, 4073–4085. https://doi.org/10.5194/bg-10-4073-2013.

Jackson, C., 2004. An Atlas of Internal Solitary-like Waves and Their Properties. Global Ocean Associates, Alexandria, Va, 2004.

Jackson, J.M., Rainville, L., Roberts, M.J., McQuaid, C.D., Lutjeharms, J.R.E., 2012. Mesoscale bio-physical interactions between the Agulhas current and the Agulhas Bank, South Africa. Continent. Shelf Res. 49, 10–24. https://doi.org/10.1016/j.csr.2012.09.005.

Krug, M., Penven, P., 2011. New perspectives on Natal Pulses from satellite observations. J. Geophys. Res.: Oceans 116. https://doi.org/10.1029/2010JC006866.

Lampitt, R.S., 1985. Evidence for the seasonal deposition of detritus to the deep-sea floor and its subsequent resuspension. Deep Sea Res. Part A. Oceanogr. Res. Pap. 32, 885–897. https://doi.org/10.1016/0198-0149(85)90034-2.

Legendre, P., Legendre, L., 1998. Numerical Ecology, 2nd Englis. Elsevier, Amsterdam.

Lorenzen, C.J., 1966. A method for the continuous measurement of in vivo chlorophyll concentration. Deep Sea Res. Oceanogr. Abstr. 13, 223–227. https://doi.org/10.1016/0011-7471(66)91102-8.

Lutjeharms, J.R.E., Roberts, H.R., 1988. The Natal pulse: an extreme transient on the Agulhas Current. J. Geophys. Res.: Oceans 93, 631–645. https://doi.org/10.1029/JC093iC01p00631.

Lutjeharms, J.R., Cooper, J., Roberts, M., 2000. Upwelling at the inshore edge of the Agulhas current. Continent. Shelf Res. 20, 737–761. https://doi.org/10.1016/S0278-4343(99)00092-8.

Malan, N., Backeberg, B., Biastoch, A., Durgadoo, J.V., Samuelsen, A., Reason, C., Hermes, J., 2018. Agulhas current meanders facilitate shelf-slope exchange on the eastern Agulhas Bank. J. Geophys. Res.: Oceans 123, 4762–4778. https://doi.org/10.1029/2017JC013602.

Malongweni, N.V., Giering, S.L.C., Noyon, M., Rocke, E., Roberts, M., 2022. Vertical Biogeochemical Fluxes in the Agulhas Bank (Unpublished manuscript).

Mazwane, S.L., Poulton, A.J., Hickman, A., Jebri, F., Jacobs Z., Roberts, M., Noyon, M. This issue. Seasonal and long-term stability of net primary production on the Agulhas Bank, 1998 - 2018. Deep Sea Res. Part II Top. Stud. Oceanogr..

McCave, I.N., 2009. Nepheloid layers. In: Encyclopedia of Ocean Sciences. Elsevier, pp. 8–18. https://doi.org/10.1016/B978-012374473-9.00671-8.

Miller, D.C.M., Moloney, C.L., van der Lingen, C.D., Lett, C., Mullon, C., Field, J.G., 2006. Modelling the effects of physical–biological interactions and spatial variability in spawning and nursery areas on transport and retention of sardine Sardinops sagax eggs and larvae in the southern Benguela ecosystem. J. Mar. Syst. 61, 212–229. https://doi.org/10.1016/j.jmarsys.2005.03.007.

Moore, C.M., Seeyave, S., Hickman, A.E., Allen, J.T., Lucas, M.I., Planquette, H., Pollard, R.T., Poulton, A.J., 2007. Iron–light interactions during the CROZet natural iron bloom and EXport experiment (CROZEX) I: phytoplankton growth and photophysiology. Deep Sea Res. Part II Top. Stud. Oceanogr. 54, 2045–2065. https://doi.org/10.1016/j.dsr2.2007.06.011.

Noyon, M., 2019. Ellen Khuzwayo EK188 - Cruise Summary Report. Southampton.

Noyon, M., Poulton, A.J., Asdar, S., Weitz, R., Giering, S.L.C., 2022. Mesozooplankton community distribution on the Agulhas Bank in autumn: size structure and production. Deep Sea Res. Part II Top. Stud. Oceanogr. 195, 105015 https://doi.org/10.1016/j.dsr2.2021.105015.

Oksanen, J., Blanchet, F.G., Friendly, M., Kindt, R., Legendre, P., McGlinn, D., Minchin, P.R., O'Hara, R.B., Simpson, G.L., Solymos, P., Stevens, M.H.H., Szoecs, E., Wagner, H., 2016. Vegan: Community Ecology Package.

Poulton, A.J., Mazwane, S.L., Godfrey, B., Carvalho, A., Mawji, E., Wihsgott, J.U., Noyon, M. This issue. Primary production dynamics on the Agulhas Bank in autumn (March 2019). Deep Sea Res. Part II Top. Stud. Oceanogr..

Poulton, A.J., Davis, C.E., Daniels, C.J., Mayers, K.M.J., Harris, C., Tarran, G.A., Widdicombe, C.E., Woodward, E.M.S., 2019. Seasonal phosphorus and carbon dynamics in a temperate shelf sea (Celtic Sea). Prog. Oceanogr. 177, 101872 https://doi.org/10.1016/j.pocean.2017.11.001.

Probyn, T.A., Mitchellinnes, B.A., Brown, P.C., Hutchings, L., Carter, R.A., 1994. Review of primary production and related processes on the Agulhas-Bank. South Afr. J. Sci. 90, 166–173.

R Core Team, 2018. R: A Language and Environment for Statistical Computing. R Foundation for Statistical Computing.

Roberts, M.J., Sauer, W.H.H., 1994. Environment: the key to understanding the South African chokka squid (Loligo vulgaris reynaudii) life cycle and fishery? Antarct. Sci. 6, 249–258. https://doi.org/10.1017/S0954102094000386.

Schallenberg, C., Harley, J.W., Jansen, P., Davies, D.M., Trull, T.W., 2019. Multi-year observations of fluorescence and backscatter at the southern ocean time series (SOTS) shed light on two distinct seasonal bio-optical regimes. Front. Mar. Sci. 6 https://doi.org/10.3389/fmars.2019.00595.

Schumann, E.H., Brink, K.H., 1990. Coastal-trapped waves off the coast of South Africa: generation, propagation and current structures. J. Phys. Oceanogr. 20, 1206–1218. https://doi.org/10.1175/1520-0485(1990)020<1206:CTWOTC>2.0.CO;2.

Sink, K., Holness, S., Harris, L., Majiedt, P., Atkinson, L., Robinson, T., Kirkman, S., Hutchings, L., Leslie, R., Lamberth, S., Kerwath, S., von der Heyden, S., Lombard, A., Attwood, C., Branch, G., Fairweather, T., Taljaard, S., Weerts, S., Cowley, P., Wolf, T., 2012. National Biodiversity Assessment 2011: Technical Report (Volume 4). Marine and Coastal Component. South African National Biodiversity Institute, Pretoria.

Stramski, D., Boss, E., Bogucki, D., Voss, K.J., 2004. The role of seawater constituents in light backscattering in the ocean. Prog. Oceanogr. 61, 27–56. https://doi.org/10.1016/j.pocean.2004.07.001.

Sullivan, J.M., Twardowski, M.S., Ronald, J., Zaneveld, V., Moore, C.C., 2013. Measuring optical backscattering in water. In: Light Scattering Reviews 7. Springer Berlin Heidelberg, Berlin, Heidelberg, pp. 189–224. https://doi.org/10.1007/978-3-642-21907-8_6.

Thompson, C.E.L., Williams, M.E., Amoudry, L., Hull, T., Reynolds, S., Panton, A., Fones, G.R., 2019. Benthic controls of resuspension in UK shelf seas: implications for resuspension frequency. Continent. Shelf Res. 185, 3–15. https://doi.org/10.1016/j.csr.2017.12.005.

Tian, Z., Jia, Y., Chen, J., Liu, J.P., Zhang, S., Ji, C., Liu, X., Shan, H., Shi, X., Tian, J., 2021a. Internal solitary waves induced deep-water nepheloid layers and seafloor geomorphic changes on the continental slope of the northern South China Sea. Phys. Fluids 33, 053312. https://doi.org/10.1063/5.0045124.

Tian, Z., Jia, Y., Du, Q., Zhang, S., Guo, X., Tian, W., Zhang, M., Song, L., 2021b. Shearing stress of shoaling internal solitary waves over the slope. Ocean Eng. 241, 110046 https://doi.org/10.1016/j.oceaneng.2021.110046.

Tian, Z., Jia, Y., Zhang, S., Zhang, X., Li, Y., Guo, X., 2019. Bottom and intermediate nepheloid layer induced by shoaling internal solitary waves: impacts of the angle of the wave group velocity vector and slope gradients. J. Geophys. Res. Ocean. 124, 5686–5699. https://doi.org/10.1029/2018JC014721.

Townsend, D.W., Mayer, L.M., Dortch, Q., Spinrad, R.W., 1992. Vertical structure and biological activity in the bottom nepheloid layer of the Gulf of Maine. Continent. Shelf Res. 12, 367–387. https://doi.org/10.1016/0278-4343(92)90037-K.

Villa-Alfageme, M., de Soto, F.C., Ceballos, E., Giering, S.L.C., Le Moigne, F.A.C., Henson, S., Mas, J.L., Sanders, R.J., 2016. Geographical, seasonal, and depth variation in sinking particle speeds in the North Atlantic. Geophys. Res. Lett. 43, 8609–8616. https://doi.org/10.1002/2016GL069233.

Welschmeyer, N.A., 1994. Fluorometric analysis of Chlorophyll-a in the presence of Chlorophyll-b and pheopigments. Limnol. Oceanogr. 39, 1985–1992.

Whittle, C., Lutjeharms, J.R.E., Duncombe Rae, C.M., Shillington, F.A., 2008. Interaction of Agulhas filaments with mesoscale turbulence: a case study. South Afr. J. Sci. 104, 135–139.

Wilkinson, S., Japp, D.W., 2005. Description and Evaluation of Hake-Directed Trawling Intensity on Benthic Habitat in South Africa. Cape Town.

Zhang, X., Hu, L., He, M.-X., 2009. Scattering by pure seawater: effect of salinity. Opt Express 17, 5698. https://doi.org/10.1364/OE.17.005698.

Zoutendyk, P., Duvenage, I.R., 1989. Composition and biological implications OF a nepheloid layer over the inner Agulhas Bank near mossel bay, South Africa. Trans. Roy. Soc. S. Afr. 47, 187–197. https://doi.org/10.1080/00359198909520162.